Tomography of Materials and Structures 10 (2026) 100081

Contents lists available at ScienceDirect

Tomography of Materials and Structures

journal homepage: www.journals.elsevier.com/tomography-of-materials-and-structures

A flexible deconvolution-based reconstruction pipeline for edge illumination phase-contrast computed tomography

Giada Rizzo [a,c], Luca Brombal [b,c,*], Francesco Brun [a,c]

[a] Department of Engineering and Architecture, University of Trieste, Trieste, Italy
[b] Department of Physics, University of Trieste, Trieste, Italy
[c] National Institute for Nuclear Physics (INFN), Trieste Division, Trieste, Italy

ARTICLE INFO

Keywords:
X-ray Phase Contrast Tomography
Differential Phase Contrast
Differential Phase Integration
Edge Illumination
Deconvolution

ABSTRACT

Differential phase contrast (DPC) computed tomography (CT), such as Edge Illumination (EI) CT, traditionally incorporates phase integration into the tomographic reconstruction process using Hilbert filtering followed by backprojection. Although this approach is fast, effective, and parameter-free, it offers limited flexibility for noise handling and precludes the use of algebraic reconstruction methods. In this work, we reformulate the phase integration step as a deconvolution problem and propose a practical pipeline that preserves the quantitativeness of phase contrast data as well as enables the use of algebraic reconstruction techniques. We demonstrate and compare several deconvolution strategies on both simulated and experimental data. Qualitative and quantitative evaluations consistently highlight the advantages of the proposed approach.

1. Introduction

X-ray phase contrast imaging (XPCI) is a technique that holds significant potential to enhance image quality beyond what conventional attenuation-based imaging can achieve. Unlike traditional methods, XPCI is sensitive to the phase shifts that X-rays experience as they pass through a sample, enabling improved contrast—particularly for materials with low absorption. The interaction of X-rays with matter is described by the complex refractive index $n = 1 - \delta + \beta$, which accounts both phase (δ) and attenuation (β) effects. For light materials and at energies of interest in X-ray imaging (10 – 100 keV), the phase shift component is significantly larger than the absorption term, resulting in phase images that exhibit higher contrast-to-noise ratio compared to conventional absorption-based images [1]. Moreover, phase-shift effects occurring at spatial scales smaller than the system's resolution contribute to the dark-field signal, which encodes information about the microscopic structure of features that are not spatially resolved within the sample. Thanks to this advantage, XPCI is gaining increasing prominence, and several methods have been developed to exploit phase contrast, including edge illumination (EI) and grating interferometry techniques [2–4]. These approaches enable the simultaneous acquisition of three contrast mechanisms in a single scan: conventional absorption contrast, differential phase contrast (DPC), and small-angle scattering contrast, also known as dark-field. DPC captures the first derivative of the phase shift due to the sample, along a single direction determined by the experimental configuration. In an typical EI setup, the absorption mask with vertical periodic structures generates unidirectional DPC with phase sensitivity along the horizontal direction, enhancing the visualization of edges and fine structural details within the sample. However, DPC does not directly provide a quantitative phase map, requiring a phase retrieval step to reconstruct the full phase information.

In computed tomography (CT), an analytic solution to the phase integration problem is achieved by applying Hilbert filtering to the projections prior to reconstruction via back projection (BP). In general, this provides the solution for all differential phase imaging methods with phase sensitivity oriented orthogonally to the rotation axis. This approach, detailed in [5] and applied to grating interferometry data, is both effective and computationally efficient. However, it has limited adaptability under high-noise conditions due to the absence of tuning parameters. Moreover, it constrains the reconstruction method to FBP exclusively, restricting the use of alternative reconstruction strategies. In contrast, 3D algebraic reconstruction methods, such as the Simultaneous Iterative Reconstruction Technique (SIRT), Conjugate Gradient Least Squares (CGLS), or Fast Iterative Shrinkage-Thresholding Algorithm (FISTA), are better suited for high-noise, sparse-sampling, and

* Correspondence to: Department of Physics, University of Trieste, Via Alfonso Valerio, 2, Trieste, TS 34127, Italy.
E-mail address: lbrombal@units.it (L. Brombal).

https://doi.org/10.1016/j.tmater.2025.100081
Received 27 August 2025; Received in revised form 9 November 2025; Accepted 16 December 2025
Available online 30 December 2025

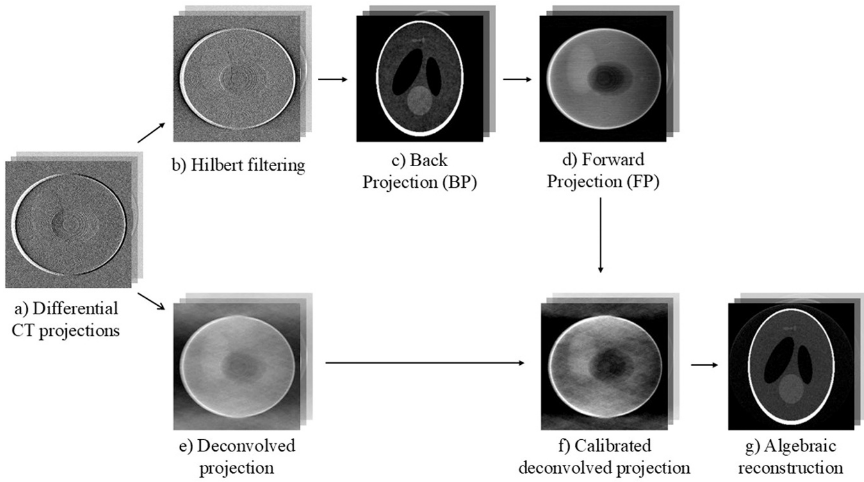

Fig. 1. Sketch of the proposed processing pipeline: differential CT projections (a) are processed using Hilbert filtering (b) to obtain the reconstruction shown in (c). In parallel, the projections are also processed via deconvolution (e), and then calibrated (f) using the gray-level histogram of the forward projections of the previously Hilbert-filtered reconstruction (d). The calibrated dataset is subsequently used for algebraic reconstruction (g).

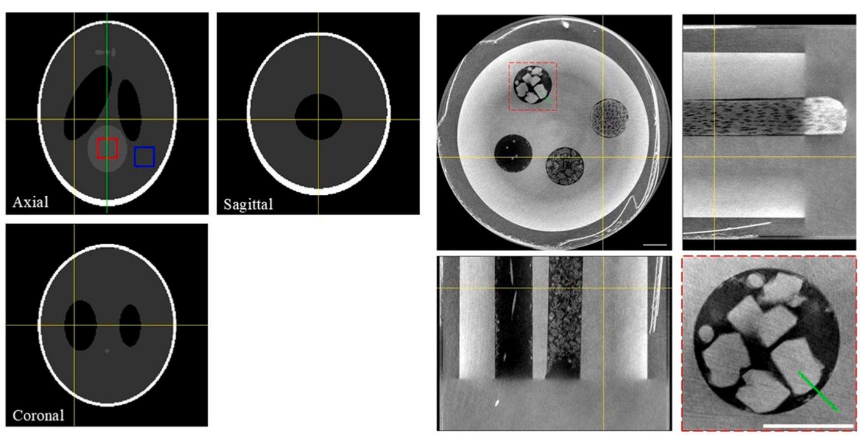

a) Simulated image b) Experimental image

Fig. 2. Both simulated (a) and experimental (b) images show a green line indicating the pixels considered for the line profile. The red and blue regions marked in the simulated image are used for the CNR calculation. [Scale bar in b) = 1 mm].

limited-angle scenarios, offering greater flexibility and robustness [6].

In this work, we propose an alternative to the Hilbert-filtered BP reconstruction, applied to EI phase contrast CT data featuring an absorbing mask with vertical, i.e. parallel to the rotation axis, apertures. We compare and discuss results from both simulated and experimental datasets. Our approach models phase integration as a discrete deconvolution of a derivative filter. This process is inherently ill-posed: integration recovers the phase only up to an unknown additive constant, and even small noise in the measured derivative can be propagated across the integrated image. This instability is especially pronounced at low spatial frequencies, where the derivative operator's frequency response approaches zero, complicating the deconvolution.

To address this, we introduce normalization approach to preserve the quantitative accuracy of the deconvolved phase. The normalization factors are derived from the forward projections of Hilbert-filtered back-projected data. The backprojection–reprojection operation helps to stabilize the ill-posed low-frequency components, since the low-frequency information is reinforced across multiple projections. In addition, this choice provides a parameter-free strategy: Hilbert filtering and reconstruction require no tuning, whereas alternative regularization approaches generally involve one or more adjustable parameters and might fail to achieve the same quantitative accuracy as the back-projection–reprojection operation. This choice is also motivated by common laboratory practice: Hilbert filtering and reconstruction are routinely performed to obtain rapid feedback on the acquisition conditions. As a result, a fast Hilbert-based reconstruction is already available and can be easily used for the normalization procedure. The overall proposed approach is illustrated in Fig. 1. With this method, any deconvolution algorithm capable of handling a derivative kernel can be employed. Since most deconvolution techniques require regularization, standard image denoising algorithms — such as BM3D, total variation (TV) denoising, or deep learning-based methods — can be integrated seamlessly. This flexibility has led to what is known as a "plug-and-play" deconvolution approach [7] (see also [8] for the origin of the term).

In this paper, we compare three strategies: a straightforward non-iterative Wiener deconvolution algorithm, a "plug-and-play" restoration incorporating simple TV denoising and a more advanced sparse deconvolution approach. Furthermore, our approach enables the use of algebraic reconstruction algorithms, which overcome common limitations of BP, such as improved noise robustness, better handling of sparse projection data, and compensation for missing projections. In this work, we compare the results of an algebraic reconstruction algorithm against

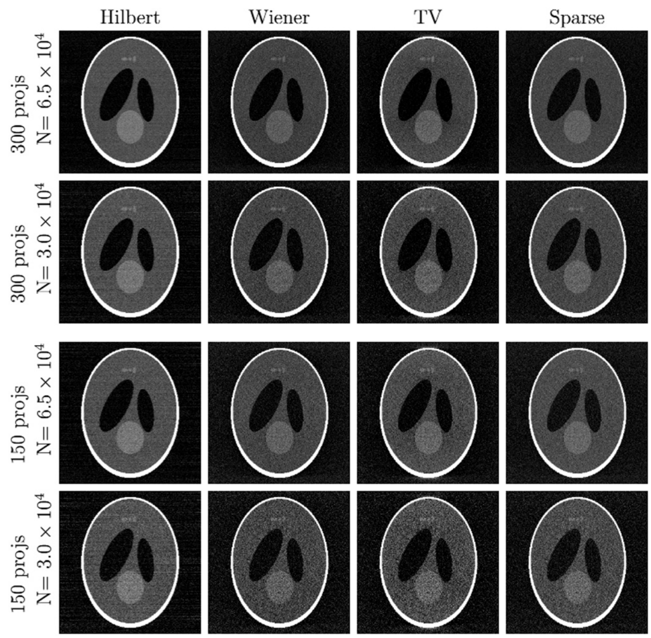

Fig. 3. Reconstructed simulated images of 256 × 256 pixels using (from left to right): Hilbert filtering and BP reconstruction, Wiener, TV, and sparse deconvolution with SIRT reconstruction. Two angular sampling scenarios are considered: a data-sufficient case with 300 projections and an under-sampled case with 150 projections. Each row corresponds to a different simulation condition (top to bottom): 300 projections with Poisson noise $N = 6.5 \bullet 10^4$, 300 projections with $N = 3.0 \bullet 10^4$, 150 projections with $N = 6.5 \bullet 10^4$, and 150 projections with $N = 3.0 \bullet 10^4$.

Hilbert-filtered BP. The proposed workflow is flexible and tunable, making it especially effective for EI-CT acquisitions affected by high noise levels and limited projection counts, conditions that typically degrade the quality of Hilbert-filtered BP reconstructions.

2. Materials and methods

2.1. Modeling

The mathematical model adopted throughout this work is described by Eq. (1), where g_θ denotes the refraction signal image at every angle θ, modeled as the convolution (represented by the operator $\star$) between the target image f_θ and the horizontal derivate kernel h. An additive noise component n is also included in the model, thus leading to:

$$g_\theta = f_\theta \star h + n \tag{1}$$

where

$$h = \begin{bmatrix} 0 & 0 & 0 \\ 0 & -1 & 1 \\ 0 & 0 & 0 \end{bmatrix}.$$

This model is used to produce simulated data as well as to perform phase retrieval, i.e. to recover an effective estimation $\widehat{f}_\theta$ of the phase image f_θ by applying suitable deconvolution algorithms to the refraction image g_θ.

2.2. Datasets

2.2.1. Simulated dataset

The simulated data are generated using a 3D Shepp-Logan phantom, resulting in a volumetric image of 256 × 256 × 256 voxels. The acquisition is simulated over 180° using parallel beam geometry. To produce a differential phase contrast CT dataset, each projection from the CT simulation is convoluted with the horizontal derivative matrix described in Eq. (1) and Poisson noise is added to the differential projections.

2.2.2. Experimental dataset

The experimental dataset consists of images acquired at [9] using a double mask edge illumination configuration in cone beam geometry. X-rays are generated by a fixed tungsten anode microfocus tube (Hamamatsu L10101) operating at voltages between 40 and 100 kVp and currents between 10 and 200 μA. The experimentally characterized focal spot dimension is in the range from 5 to 30 μm. The imaging detector is a Pixirad-1/Pixie-III photon-counting device, featuring a 650 μm thick CdTe sensor bump bonded on a 512 × 402 matrix of pixels with a size of 62 μm, corresponding to an active area of 31.7 × 24.9 mm^2. The dataset consisted of 720 projections acquired at 50 kVp and 150 μA, with an exposure time of 4.5 s and 6 dithering steps, and without any additional beam filtration. The sample is a cylindrical PMMA object containing four holes filled with kitchen salt, flour, coffee powder, and a toothpick, respectively. Preprocessing of the acquired differential projections includes correction for hot and dead pixels and normalization of the mean intensity to zero. The final reconstruction yields a volumetric dataset composed of several 2D slices of 994 × 994 pixels, with a pixel size of 0.01 mm.

2.3. Deconvolution algorithms

2.3.1. Wiener deconvolution

The Wiener filter is a linear method that enables an effective estimation $\widehat{f}_\theta$ of the function f_θ without requiring an iterative approach. Eq. (2) illustrates the approach where λ represents the regularization parameter and H the frequency response of the filter, i.e. the Fourier transform of the derivative kernel h.

$$\widehat{f} = \mathscr{F}^{-1}\left\{\mathscr{F}\{g\}\cdot\frac{H^*}{|H|^2 + \lambda}\right\} \tag{2}$$

The regularization parameter can be defined either as a constant or as a frequency-dependent function. In the simulated dataset, a constant value is selected for the parameter λ. For the experimental dataset, as suggested in [10], a Butterworth filter — described in Eq. (3) — is employed to achieve an improved response at high spatial frequencies. To mitigate unidirectional streak artifacts, only the vertical frequency component ν is considered, where ν_0 denotes the vertical cutoff frequency.

$$\lambda(\nu) = \frac{1}{1 + \left(\frac{\nu}{\nu_0}\right)^{2n}} \tag{3}$$

2.3.2. "Plug and play" deconvolution with TV denoiser

This approach follows the description reported in [8] where an Alternating Direction Method of Multiplier (ADMM) is used to solve the deconvolution problem. As a regularizer, a simple Total Variation denoiser with tuning parameter λ is included, being quite common in this context (see e.g. [11]). The overall approach for each acquired projection image g_θ is shown in Eq. (4)

$$\widehat{f}_\theta = \underset{f_\theta}{\operatorname{argmin}}\left(|h * f_\theta - g_\theta|_2^2 + \lambda|f_\theta|_{TV}\right) \tag{4}$$

where

$$||f_\theta||_{TV} = \sum_{x,y}\sqrt{\left(\frac{\partial f_\theta}{\partial x}\right)^2 + \left(\frac{\partial f_\theta}{\partial y}\right)^2} \tag{5}$$

being $\frac{\partial f_\theta}{\partial x}$ and $\frac{\partial f_\theta}{\partial y}$ the horizontal and vertical image gradients, respectively and (x,y) the image spatial coordinates. The first term of the equation ensures the optimal fit of the model to the observed image, by

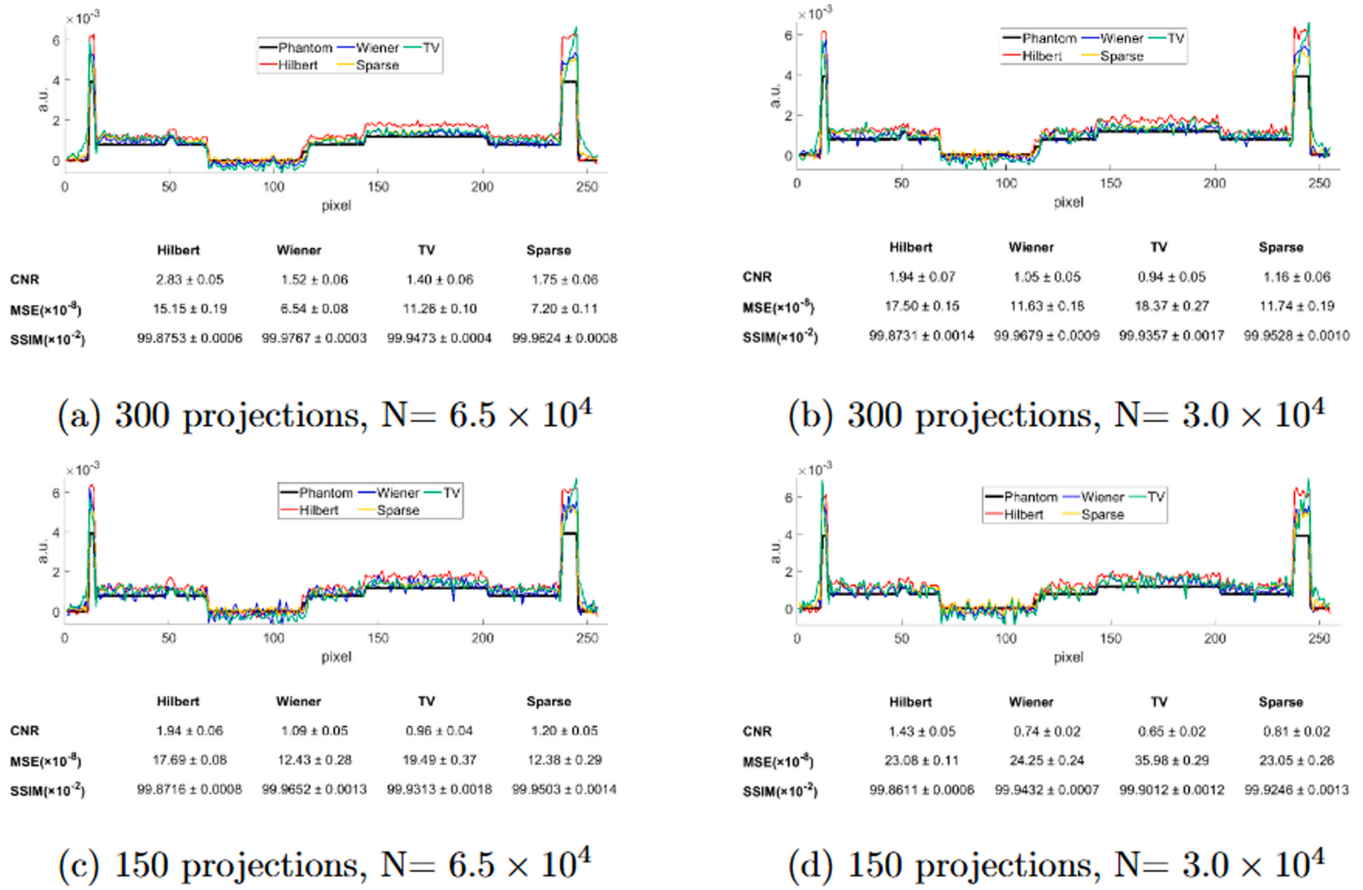

(a) 300 projections, N= 6.5×10^4

	Hilbert	Wiener	TV	Sparse
CNR	2.83 ± 0.05	1.52 ± 0.06	1.40 ± 0.06	1.75 ± 0.06
MSE($\times 10^{-8}$)	15.15 ± 0.19	6.54 ± 0.08	11.26 ± 0.10	7.20 ± 0.11
SSIM($\times 10^{-2}$)	99.8753 ± 0.0006	99.9767 ± 0.0003	99.9473 ± 0.0004	99.9624 ± 0.0008

(b) 300 projections, N= 3.0×10^4

	Hilbert	Wiener	TV	Sparse
CNR	1.94 ± 0.07	1.05 ± 0.05	0.94 ± 0.05	1.16 ± 0.06
MSE($\times 10^{-8}$)	17.50 ± 0.15	11.63 ± 0.18	18.37 ± 0.27	11.74 ± 0.19
SSIM($\times 10^{-2}$)	99.8731 ± 0.0014	99.9679 ± 0.0009	99.9357 ± 0.0017	99.9528 ± 0.0010

(c) 150 projections, N= 6.5×10^4

	Hilbert	Wiener	TV	Sparse
CNR	1.94 ± 0.06	1.09 ± 0.05	0.96 ± 0.04	1.20 ± 0.05
MSE($\times 10^{-8}$)	17.69 ± 0.08	12.43 ± 0.28	19.49 ± 0.37	12.38 ± 0.29
SSIM($\times 10^{-2}$)	99.8716 ± 0.0008	99.9652 ± 0.0013	99.9313 ± 0.0018	99.9503 ± 0.0014

(d) 150 projections, N= 3.0×10^4

	Hilbert	Wiener	TV	Sparse
CNR	1.43 ± 0.05	0.74 ± 0.02	0.65 ± 0.02	0.81 ± 0.02
MSE($\times 10^{-8}$)	23.08 ± 0.11	24.25 ± 0.24	35.98 ± 0.29	23.05 ± 0.26
SSIM($\times 10^{-2}$)	99.8611 ± 0.0006	99.9432 ± 0.0007	99.9012 ± 0.0012	99.9246 ± 0.0013

Fig. 4. Line profiles, CNR, MSE and SSIM values for each case, using 300 (a-b) and 150 (c-d) projections under two different Poisson noise levels. Each metric is derived by averaging five consecutive axial slices, and the associated error represents the standard deviation across these five measurements.

minimizing the L2-norm. The second term represents the Total Variation norm, defined as the gradient magnitude of the image f_θ, as shown in Eq. (5), multiplied by the regularization parameter λ.

2.3.3. Sparse deconvolution

To recover each image f_θ from its convolved observation g_θ, an additional method here used is the sparse prior deconvolution described by Levin et al. [12]. The approach formulates the inverse problem as a maximum a posteriori (MAP) estimation, combining a data fidelity term with a sparsity-promoting prior on filtered versions of the solution. Specifically, the method minimizes the following energy functional:

$$||h * f_\theta - g_\theta||^2 + \lambda \sum_k \rho((d_k * f_\theta)) \tag{6}$$

where ($\rho(u) = |u|^{0.8}$) is a heavy-tailed penalty function promoting sparsity in the filter responses. The set of filters $\{d_k\}$ includes first- and second-order finite difference operators. The optimization is performed using Iteratively Reweighted Least Squares (IRLS), where each iteration solves a weighted least-squares problem with weights updated based on the current estimate of f_θ. Each linear system is solved in the spatial domain using the Conjugate Gradient method. This method effectively restores sharp features and suppresses noise in the reconstructed f_θ.

2.3.4. Parameters optimization

A regularization parameter must be chosen, denoted in all the previously reported method as λ. This parameter was optimized on the simulated dataset with 150 projections and Poisson noise, assuming a total photon count $N = 6.5 \bullet 10^4$, by identifying the value that minimizes the Mean Square Error (MSE): $\lambda = 5.0 \times 10^{-2}$ for TV deconvolution, $\lambda = 2.0 \times 10^{-4}$ for sparse deconvolution, and $\lambda = 1.0 \times 10^{-4}$ for Wiener deconvolution. For the iterative deconvolution methods (TV and sparse), the number of iterations was set to 400. The same optimal value and iteration number are then applied to the experimental dataset. An exception is made for the Wiener filter used on the experimental dataset, which employs two frequency-dependent tunable parameters, whereas only a single regularization parameter is used for the simulated data. This choice is made to obtain higher-quality reconstructed images while minimizing the introduction of artifacts.

2.4. Calibration

Defined through the sign function of the horizontal frequency variable u, the Hilbert transform is employed as a filter in the filtered back-projection (FBP) image reconstruction, as described in Eq. (7). This approach is involved to reconstruct image $\hat{f}_\theta$ from the derivative data g_θ.

$$\hat{f}_\theta = \mathscr{F}^{-1}\{-i \cdot \mathrm{sgn}(u) \cdot \mathscr{F}\{g_\theta\}\} \tag{7}$$

The images reconstructed using Hilbert filtering and BP are taken as reference. A forward projection is applied to those reconstructed images to extract calibration values. To be specific, the 1st and the 99th percentiles gray values are computed. These values are then used to normalize the projections obtained from the deconvolution filters. This calibration procedure is consistently applied to both the simulated and the experimental datasets.

2.5. Reconstruction algorithm

In order to demonstrate the possibility to consider algebraic reconstruction approaches, in this work the implementation of SIRT (Simultaneous Iterative Reconstruction Algorithm) available in the open

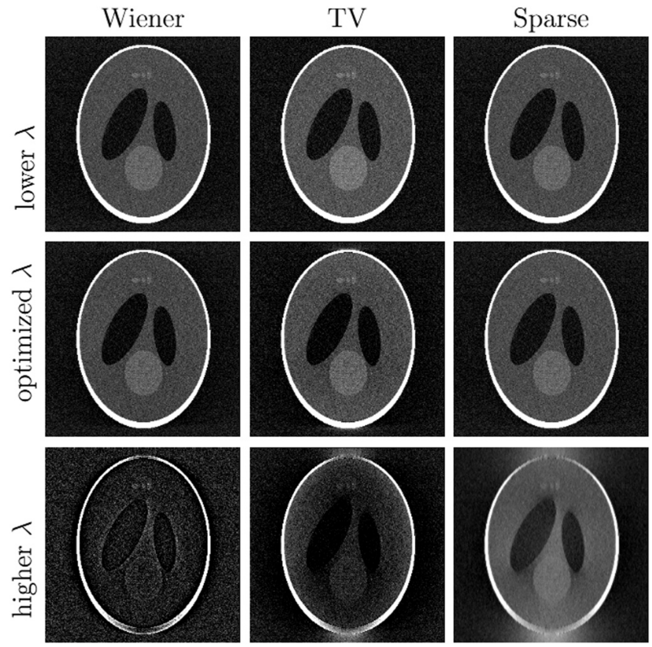

Fig. 5. Reconstructed simulated images for the scenario with 150 projections and the lower of the two noise levels considered, using different regularization parameters for each deconvolution algorithm. From top to bottom: reconstruction with a lower regularization parameter than the optimal value (Wiener: $\lambda = 1.0 \times 10^{-5}$; sparse: $\lambda = 2.0 \times 10^{-5}$; TV: $\lambda = 2.0 \times 10^{-4}$); reconstruction with the optimal regularization parameter minimizing the mean squared error (Wiener: $\lambda = 1.0 \times 10^{-4}$; sparse: $\lambda = 2.0 \times 10^{-4}$; TV: $\lambda = 5.0 \times 10^{-2}$); reconstruction with a higher regularization parameter than the optimal value (Wiener: $\lambda = 5.0 \times 10^{-2}$; sparse: $\lambda = 8.0 \times 10^{-1}$; TV: $\lambda = 8.0 \times 10^{-1}$).

source software TIGRE has been used [13]. It is implicit that any algebraic reconstruction algorithm can be included into the pipeline. In this work, only one reconstruction algorithm is used in order to have a fair quantitative comparison of the deconvolution approaches.

2.6. Quantitative analysis

Line profiles, extracted along the green line highlighted in Fig. 2, for both the simulated and experimental images, are compared. Being this work aimed for CT, only final reconstructed slices are quantitatively evaluated instead of projections. The contrast to noise ratio (CNR) has been also computed by considering the red and blue regions of interest (ROIs) defined in Fig. 2 and applying Eq. (8) where μ and σ are the mean and standard deviation gray levels within ROI_1 and ROI_2, respectively.

$$\mathrm{CNR} = \frac{|\mu_1 - \mu_2|}{\sqrt{\sigma_1^2 + \sigma_2^2}} \tag{8}$$

The mean square error (MSE) and Structural Similarity Index Measure (SSIM) [14] with respect to the ground truth (the phantom) are also reported for the simulated dataset. Quantitative results are derived by averaging five consecutive axial slices in order to reduce noise-induced variability and the error reported is the standard deviation of these five measurements.

3. Results and discussion

Qualitative and quantitative results across all scenarios are presented in Fig. 3 and Fig. 4, where theoretically optimal regularization values are employed for each deconvolution algorithm. The advantage of using deconvolution algorithms with tunable parameters, compared to the Hilbert transform, is illustrated in Fig. 5. This figure shows reconstructed images obtained using deconvolution-based algorithms with regularization parameters intentionally set below and above the optimal value. While reconstructions with lower than optimal parameters exhibit

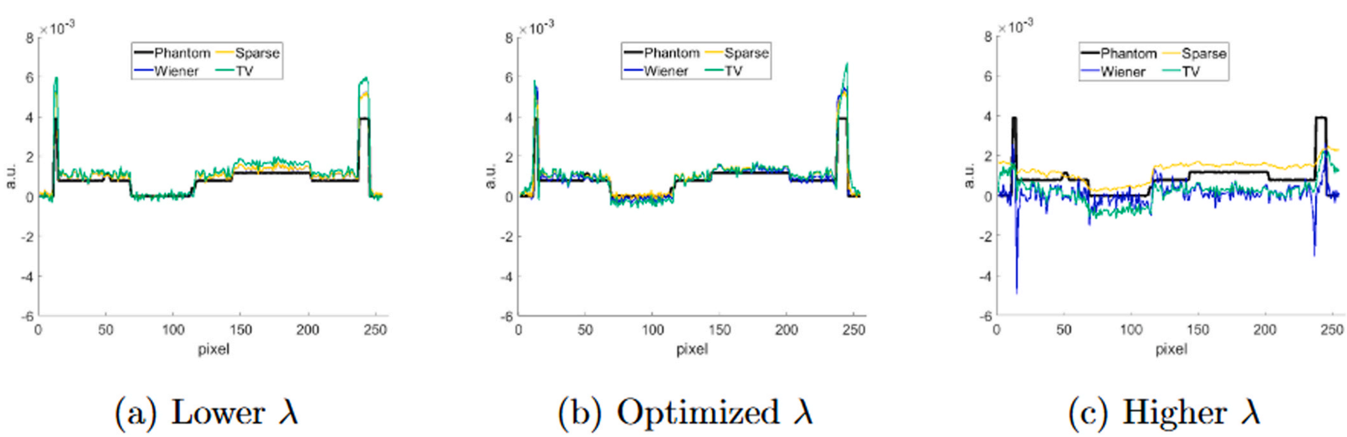

Fig. 6. Line profiles of simulated data reconstructed via phase integration after deconvolution, using different values of the regularization parameter λ: (a) lower than the optimal value, (b) the optimized value, and (c) higher than the optimal value.

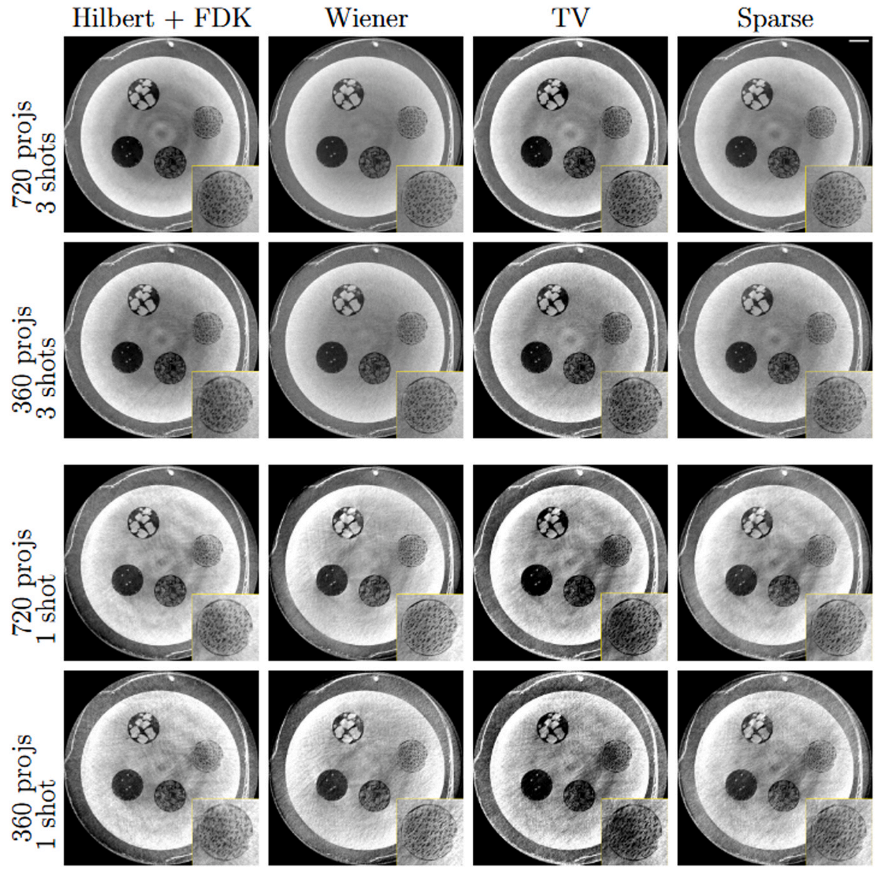

Fig. 7. Reconstructed images using (from left to right): Hilbert filtering and conventional cone-beam FDK, Wiener filter, TV deconvolution, and sparse deconvolution. The latter three images are processed according to the approach of Fig. 1 with cone-beam SIRT reconstruction. Each row corresponds to a different acquisition condition (from top to bottom): 720 projections with 3 shots per projection, 360 projections with 3 shots, 720 projections with 1 shot, and 360 projections with 1 shot. [Scale bar = 1 mm].

minimal differences compared to those with optimal values, increasing the regularization parameter significantly degrades image quality, introducing noticeable artifacts.

This is supported by the line profiles shown in Fig. 6, corresponding to reconstructions obtained using both optimal and non-optimal regularization parameters. In particular, when the parameter is overestimated, the line profile noticeably deviates from that of the original phantom, indicating the presence of artifacts. These results demonstrate the potential to improve image quality by tuning the regularization parameter, but also highlight the importance of selecting an appropriate value to balance noise suppression and artifact avoidance. In practice, this choice is not overly demanding, since under-regularization is generally less detrimental than over-regularization and relatively low values usually provide a safe compromise.

The "optimal" value reported here was derived from a theoretical assessment based on a phantom study with Poisson noise ($N = 6.5 \bullet 10^4$); therefore, the values considered in Fig. 5 and Fig. 6 do not apply universally to every acquisition but rather indicates the order of magnitude for a safe operating range. The calibration of a tunable regularization parameter represents an effective strategy to mitigate reconstruction artifacts in the presence of high noise levels. In contrast to the parameter-free Hilbert approach, deconvolution-based algorithms with adaptive regularization enhance noise suppression while preserving spatial detail. The deconvolution filter inherently behaves as a low-pass operator, attenuating high-frequency noise components. Conversely, the Hilbert filter lacks such low-pass characteristics, and residual noise therefore remains visible after reconstruction. Furthermore, normalizing the deconvolved projections with respect to Hilbert-derived forward projections helps to mitigate the ill-posedness at low spatial frequencies, since these components are redundantly sampled across multiple projections. This normalization ensures the quantitative accuracy of the reconstructed phase. The Hilbert-based reconstruction yields good quality when the noise level is low and the number of projections is sufficient. Even with a reduced number of projections, it is still capable of maintaining good performance. However, when both the number of projections is low and the noise level is high, the Hilbert filter fails to adequately compensate, resulting in images with significant noise. The corresponding line profile generally follows the trend of the original phantom, although it overestimates pixel intensity values in several regions. Deconvolution-based algorithms provide good image quality under low-noise conditions and demonstrate superior noise control compared to the Hilbert filtering BP reconstruction under adverse conditions. This is corroborated by the line profile plots, which, despite minor fluctuations, closely follow the original phantom and consistently outperform the Hilbert-based approach. Although the Hilbert filter provides higher CNR values, the deconvolution algorithms consistently achieve superior SSIM values compared to the Hilbert approach across all scenarios, including cases with fewer projections and higher noise levels. Moreover, both Wiener and sparse deconvolution yield lower MSE values than the Hilbert filter, with the exception of Wiener deconvolution under conditions of high noise and a limited number of projections. Both deconvolution methods outperform the Hilbert filter, exhibiting reduced fluctuations among slices, indicated by the error accompanying each reported CNR value. In particular, sparse deconvolution also achieves higher contrast-to-noise ratio (CNR) values compared to the other deconvolution methods, although its MSE is not lower than that of Wiener deconvolution. In contrast, total variation deconvolution provides high-quality results only under favorable

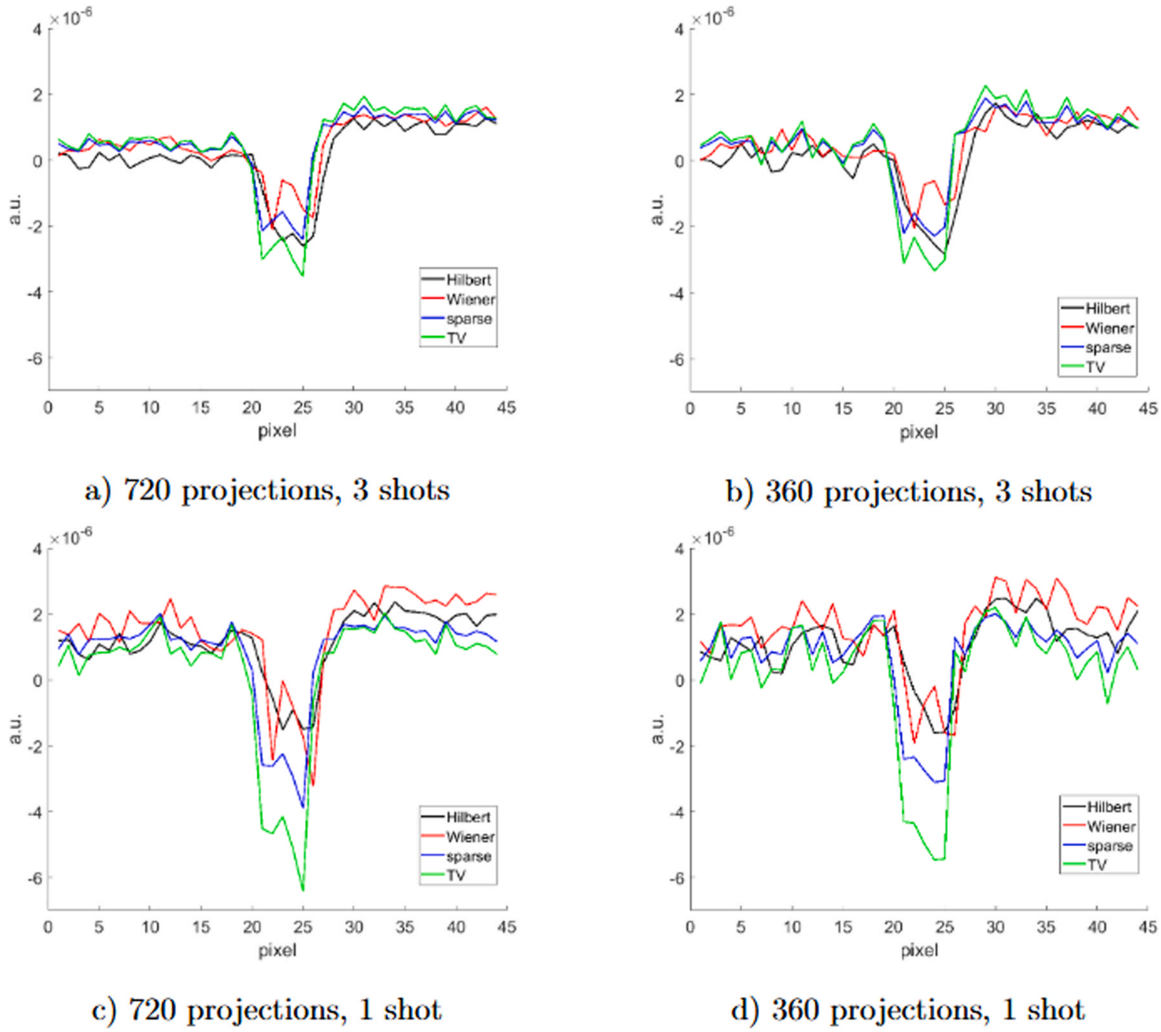

Fig. 8. Line profiles of experimental image reconstruction with 720 projections (a-c) and 360 projections (b-d) using Hilbert filtering, Wiener deconvolution, sparse deconvolution and TV deconvolution.

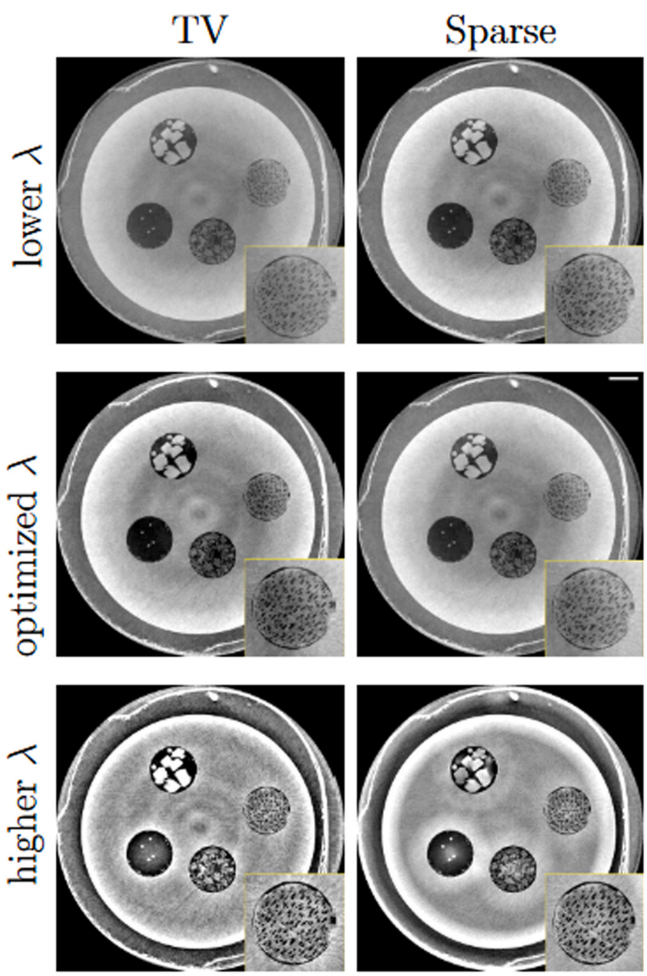

Fig. 9. Reconstructed images using different regularization parameters, corresponding to the values reported in Fig. 5 for each deconvolution algorithm (top to bottom): reconstruction with a regularization parameter lower than the optimal value; reconstruction with the optimal parameter minimizing the mean squared error (MSE); reconstruction with a regularization parameter higher than the optimal value. [Scale bar = 1 mm].

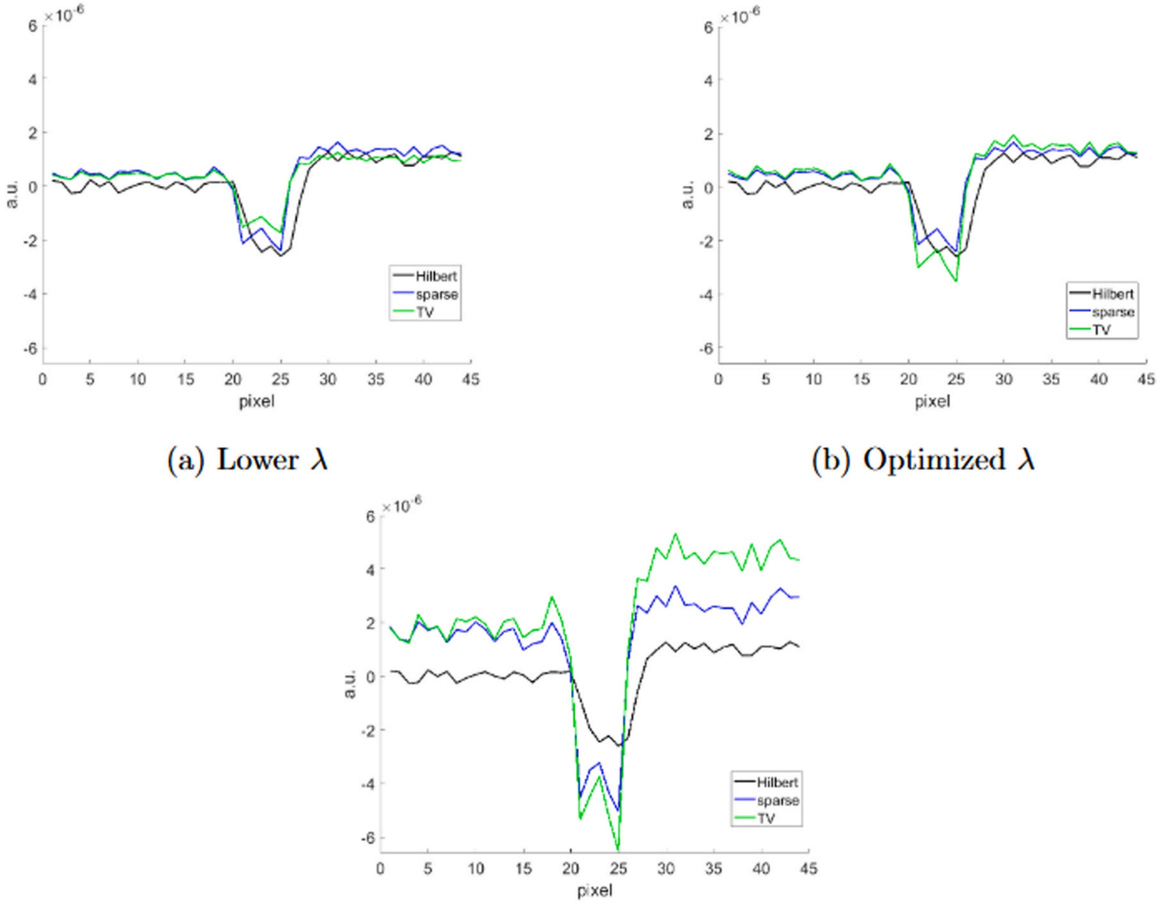

(a) Lower λ

(b) Optimized λ

(c) Higher λ

Fig. 10. Line profiles of experimental data reconstructed via phase integration after deconvolution, using different values of the regularization parameter λ: (a) lower than the optimal value, (b) the optimized value, and (c) higher than the optimal value.

conditions. These findings highlight that the proposed methodology can be effectively applied across a wide range of practical imaging conditions. By selecting the deconvolution algorithm in accordance with the specific acquisition and reconstruction settings, the approach consistently yields improved performance compared to Hilbert-based reconstruction. Reconstructed experimental images for all scenarios are shown in Fig. 7. Each figure includes a magnified region that highlights an area containing fine structures. Deconvolution-based reconstructions exhibit good image quality compared to those obtained using the Hilbert-based reconstruction, especially under low-projection conditions. None of the proposed methods introduce visible artifacts with the parameters considered, even when applied to real-world experimental data. Only the TV deconvolution method shows artifacts under such constrained conditions. The spatial resolution is also preserved, as can be seen from the line profile analyses shown in Fig. 8. In line with the simulated data, Fig. 9 shows that the use of a higher regularization parameter during the deconvolution-based integration phase leads to the appearance of artifacts, whereas setting a lower value results in minimal differences, as also corroborated by the line profiles presented in Fig. 10. Although deconvolution algorithms improve image quality, they require increased computational resources, especially for iterative methods such as sparse and TV deconvolution, compared to the Hilbert filter, which provides a rapid result. However, this limitation can be easily mitigated, as the deconvolution-based approach is highly parallelizable: each projection can be processed independently, and the use of modern GPUs allows for a significant reduction in computational time. The implementation developed in this study is available in a GitHub repository [15].

4. Conclusion

This study demonstrates the advantages of employing deconvolution-based algorithms for phase integration in differential phase contrast CT, compared to the conventional application of Hilbert-filtered back-projection (BP) reconstruction. Among the evaluated methods, sparse deconvolution consistently provides high image quality and effective noise suppression, even under limited data conditions. However, it does not outperform Wiener deconvolution, which, being a non-iterative method, could be an appealing choice when a faster reconstruction pipeline is desired. The proposed calibration approach, which relies on the forward projection of Hilbert-filtered BP-reconstructed data, preserves the quantitative accuracy of the integrated data. This methodology is also flexible, as it does not constrain the final reconstruction to be BP-based, allowing continued use of the laboratory's preferred denoising and reconstruction methods.

CRediT authorship contribution statement

Francesco Brun: Writing – review & editing, Supervision. **Luca Brombal:** Writing – review & editing, Investigation. **Giada Rizzo:** Writing – original draft.

Declaration of Competing Interest

The authors declare the following financial interests/personal relationships which may be considered as potential competing interests: Giada Rizzo reports financial support was provided by European Social Fund. Francesco Brun reports financial support by the Project of Relevant National Interest (PRIN) "Laboratory-based 3D spectral virtual histology by means of photon-counting phase-contrast X-ray computed micro-tomography (micro-CT)" [Project code: 2022HCKXPC], funded by the European Union – NextGenerationEU. If there are other authors, they declare that they have no known competing financial interests or personal relationships that could have appeared to influence the work reported in this paper.

References

[1] A. Bravin, P. Coan, P. Suortti, X-ray phase-contrast imaging: from pre-clinical applications towards clinics, Phys. Med. Biol. 58 (1) (2013).
[2] L. Massimi, T. Partridge, A. Astolfo, M. Endrizzi, C.K. Hagen, P.R.T. Munro, D. Bate, A. Olivo, Optimization of multipoint phase retrieval in edge illumination X-ray imaging. A theoretical and experimental analysis, Med. Phys. 48 (5884) (2021).
[3] A. Zamir, M. Endrizzi, C.K. Hagen, F.A. Vittoria, L. Urbani, P. De Coppi, A. Olivo, Robust phase retrieval for high resolution edge illumination x-ray phase-contrast computed tomography in non-ideal environments, Sci. Rep. 6 (31197) (2016).
[4] M. Stampanoni, Z. Wang, T. Thüring, C. David, E. Rössl, U. van Stevendaal, T. Köhler, M. Trippel, G. Singer, R.A. Kubik-Huch, M.K. Hohl, N. Hauser, Toward clinical differential phase contrast mammography: preliminary evaluations and image processing schemes, J. Instrum. 8 (C05009) (2013).
[5] D. Pelliccia, R. Vaz, I. Svalbe, K.S. Morgan, S. Marathe, X. Xiao, L. Assoufid, R. A. Anderson, J. Topczewski, R.J. Bryson-Richardson, Comparison of different numerical treatments for x-ray phase tomography of soft tissue from differential phase projections, Phys. Med. Biol. 60 (3065) (2015).
[6] J. Fu, X. Hu, A. Velroyen, M. Bech, M. Jiang, F. Pfeiffer, 3D algebraic iterative reconstruction for cone-beam X-ray differential phase-contrast computed tomography, PLOS ONE 10 (3) (2015) 1–13.
[7] J. Mulcahy-Stanislawczy, A.L. Dagel, Plug-and-play sparse X-ray phase contrast dark field tomography, IS T Int. Symp Electron. Imaging Sci. Technol. 35 (14) (2023).
[8] S.H. Chan, X. Wang, O.A. Elgendy, Plug-and-Play ADMM for image restoration: fixed-point convergence and applications, IEEE Trans. Comput. Imaging 3 (1) (2017) 84–98.
[9] L. Brombal, F. Arfelli, R. Menk, L. Rigon, F. Brun. PEPI Lab, a flexible compact multi-modal setup for X-ray phase-contrast and spectral imaging, Scientific Reports 13 (4206) (2023).
[10] L. Massimi, I. Buchanan, A. Astolfo, M. Endrizzi, A. Olivo, Fast, non-iterative algorithm for quantitative integration of X-ray differential phase-contrast images, Opt. Express 28 (26) (2020).
[11] J.I. Sperl, D. Bequé, G.P. Kudielka, K. Mahdi, P.M. Edic, C. Cozzini, A Fourier-domain algorithm for total-variation regularized phase retrieval in differential X-ray phase contrast imaging, Opt. Express 22 (1) (2014).
[12] A. Levin, R. Fergus, F. Durand, W.T. Freeman, Image and depth from a conventional camera with a coded aperture, ACM Trans. Graph. 26 (3) (2007).
[13] A. Biguri, T. Sadakane, R. Lindroos, Y. Liu, M.S. Landman, Y. Du, M. Lohvithee, S. Kase, S. Hatamikia, R. Bryll, E. Valat, S. Wonglee, T. Blumensath, C. Schönlieb, TIGRE v3: efficient and easy to use iterative computed tomographic reconstruction toolbox for real datasets, Eng. Res. Express 7 (015011) (2025).
[14] Z. Wang, A.C. Bovik, H.R. Sheikh, E.P. Simoncelli, Image quality assessment: from error visibility to structural similarity, IEEE Trans. Image Process. 13 (4) (2004).
[15] https://github.com/francescobrun/deconvDPC.